Review

Review on Proton Exchange Membrane Fuel Cell's Metallic Bipolar Plate Fabrication Challenges

Fang-Bor Weng[1,], Mangaliso Menzi Dlamini[1], Chia-Hung Chen[2]*

[1] Department of Mechanical Engineering/Fuel cell center, Yuan Ze University, Taoyuan City 32003, Taiwan.
[2] Fucell Co. Ltd Taoyuan City, Taiwan
[*]E-mail: fangbor@saturn.yzu.edu.tw

Background: Proton exchange membrane fuel cells (PEMFCs) are promising clean energy converting device that has recently attracted the attention of many electricity-consuming industries. The substitution of graphite bipolar plates (BPs) with metallic BPs broadens PEMFC applications to vibration-dominated areas. Traditional BPs contribute approximately 30–50% to cost, 60–85% to weight, and 60–90% to the cell overall volume. *Methods:* In this study, the forming methods and critical failure characteristics of metal BPs are investigated. Stamping and pressing are common and inexpensive methods adopted in metallic BP forming. From the recorded literature, this study presents a novel hybrid forming process that is effective in mitigating thinning and dents, which are critical failure parameters. *Significant findings:* Thinning, dents, and rupture are critical failure parameters in metallic BPs. Failure is more common in bends. This state-of-the-art technique constitutes lubricated roller-fashioned dice. It is effective in both straight channels and lattice patterns. This novel technique is estimated to have a 100% feel-up ratio and 80% thinning reduction.

Keywords: Bipolar plate, Coating, Fabrication, Hybrid, Proton exchange membrane fuel cell.

1. INTRODUCTION

Hydrogen is currently a promising clean energy source for the next generation, and its potential is irrefutable. Hydrogen energy plays a massive role in military service (hydrogen bombs, fueling drones). This work is focused on hydrogen energy transformation through proton exchange membrane fuel cells (PEMFCs). A fuel cell is a device that electrochemically transforms chemical energy into electrical energy. Fuel cells come in different nature. There are, phosphoric acid fuel cell, solid oxide fuel cell, alkaline fuel cell, direct methanol fuel cell, molten carbonate fuel cell, PEMFC, just to mention a few. All these cells have different favorable application conditions. In our previous work [1], we

experimentally and numerically analyzed reversible solid oxide cells, and we learned that they require a high startup duration as they are operated at high temperatures of approximately 750 °C. In addition to the high operating temperatures, we realized that solid oxide fuel cells constitute ceramics that are not compatible with vibration-dominated applications, such as the transportation industry. PEMFCs have drawn much attention because of their short start-up duration and high power density. This has won the hearts of the automobile industry, unmanned aerial vehicles (UAVs), and other dynamic and stationery applications. PEMFCs have even been proposed for portable gadgets such as cellular phones. Although traditional PEMFCs use brittle graphite bipolar plates (BPs), the mushrooming developments of metallic BPs broaden their applications to vibration-dominated areas. Their efficiency depends on different features, including materials, design, assembly skill, and operating conditions. The design feature is a broad subject, but our work will be more focused on flow field design, which mainly constitutes the BP. BPs should ensure adequate species distribution over the active and reactive regions. This means that it should even promote species distribution, diffusion, and byproduct removal (mainly water and heat). In addition to mass transfer, BPs also serve as current conductors; therefore, that feature competes with the mass transfer features because they all demand more active areas. The GDL/BP contact surface should be well managed to ensure enough mass flow and current collection. Under stack conditions, BPs also serve as separators between cells. The anode and cathode BP property demands are not exactly the same. The channel depth is critical on the cathode side. The water generated in the cathode also intensifies the demand for deeper and larger channels. Some companies have replaced anode channels with increased anode GDL porosity and size to facilitate hydrogen flow. This study is focused on finding a means to alleviate metallic BP fabrication failure. This should come in handy with product quality and cost management.

Fuel cell applications play a conspicuous role in BP material and design selection. Most applications demand high power density with relatively low size and weight. The transportation industry has shown more interest in PEMFC technology. This is because the transportation industry is among the greatest consumers of fossil fuels, which are environmentally unfriendly [2,3]. Their objectives are light weight, reduced volume, long lifetime, high power density, high mechanical strength, minimal heat and electric resistance, and low cost. PEMFCs show good performance and lifespan when implemented on electric forklifts [4]. BPs make a prominent share of cell size, cost, shape, and quality [5]. They contributed approximately 30–50% to the cost, 60–85% to the weight, and 60–90% to the volume of the overall traditional cell [5-7]. It has to be inert, corrosion resistant, good heat and current conduction, good mechanical stability, good stress and strain durability, light weight, less volume coverage, etc. Considerable literature [8-10] has evaluated metal foam flow field. These developments dramatically improved the PEMFC performance, both in fluid distribution and current collection; although it demanded further segmentation parallel to the axial direction to evenly utilize all the MEAs. Metal foam filled flow field also has improved heat conduction [11]. Graphite further offers eminent limiting factors on BP fabrication and cell dynamic application because of its brittleness [12]. Researchers have shown increasing interest over thin metal sheets BPs.

Metallic BPs have been noted to tremendously increase the power density in PEMFCs and meet most of the former listed qualities, which makes them surpass graphite; however, corrosion is the main drawback associated with it. Corrosion attacks the metal, causing scaling and passive film accumulation

on its surface, resulting in poor contact between transition surfaces. This leads to a hike in interfacial contact resistance (ICR). If the cell consumes considerable power due to resistance hikes [13], it becomes prone to overheating, thus lowering its life span. Apart from increasing the ICR, corrosion results in substrate pitting [14], thus allowing reactant mixing. Most importantly, during corrosion, some gases are emitted during the corrosion process, thus poisoning the MEA. These factors will definitely accelerate cell degradation. Different metal materials have been considered for metallic BP fabrication. These include stainless steel (SS316, SS304, SS316 L), AA-5182 aluminum alloy, and titanium [15]. Seemingly stainless steel is taking the lead. Studies have confirmed that both ferritic and austenitic stainless steel are qualified for PEMFC BP applications [16-18], although they degrade with time, increasing the contact resistance [19]. BP design should account for generated water removal [20-22]. Water is better removed before condensation as it becomes lighter in weight and demands less removal energy.

Multistage stamping [23,24] has been instituted to alleviate necking, which is a result of excessive stretching in metallic BP forming. Multistage stamping allows for even deeper channels. Warping, spring back and wrinkling are other challenges dominating metallic BP forming [25-27]. The depth-to-width ratio (aspect ratio) has considerable effects on the success of channel forming in metallic materials. A decrease in aspect ratio improves channel depth. In a recent study, a 566 μm depth with a 0.5 aspect ratio channel was successfully produced through a hot metal gas forming process at 400 °C and 40 bar and a die corner radius of 7.5° [*28*].

The bipolar plate ICR improves with an increase in compression load because this maximizes the contact area between two transition surfaces, which increases conductivity. [13]. An increased compression load further gives resistance to the expansion force exerted by the expanding and flaking fragments on corrosion, thus maintaining the contact surface area. In PEMFC applications, the compression load can only be increased to a certain limit for optimum performance. This is attributed to cell porosity, which should not be compromised. Cell pore distribution is also dependent on compressive loading during assembly [29]. In addition to cell porosity, the BP flow field may be altered with an increase in compression load. In our previous work [1], we investigated porosity effects on reversible solid oxide fuel cells, and they concluded an optimum porosity range of 30% to 40%, which should be evenly distributed. It is of great importance to understand that anode porosity demand is different from that of the cathode. Two main factors contribute to this phenomenon. The first factor is the difference in reactant molecular size. Hydrogen constitutes a much smaller size. The second attribute is that of the generated water, which is almost in the liquid phase. Generally, water is generated on the cathode side and demands larger pores compared to that of the anode.

As renewable energy is an undoubtable effective alternative to fossil fuels, it should be well studied to ensure sustainability and durability. Nuclear power has proven to contain tremendous power density compared to fossil fuels, but on the contrary, it possesses high hazardous effects [30]. Not only to the workers but also to the whole community of it location. Its supper high half-life worsens its danger. PEMFCs impose less than 5% danger to the environment in all fabrication and operation exercises.

2. BPs WEIGHT AND VOLUME:

BPs have a remarkable contribution to the overall cell weight and volume. As mentioned in section 1, it contributes approximately 60–85% to the weight and 60–90% to the overall cell volume. Conventional graphite material BPs [12] have a relatively low cost and acceptable conductivity. In addition to these qualities, graphite is less susceptible to corrosion even under humid and acidic conditions. In general, graphite is a brittle ceramic, giving it less priority in PEMFC development. For graphite to have mechanical stability, it demands a remarkably high volume size which ends up increasing the total weight. Otherwise, when using the same thickness, graphite is less dense, thus having a relatively low weight compared to a number of metallic materials [31].
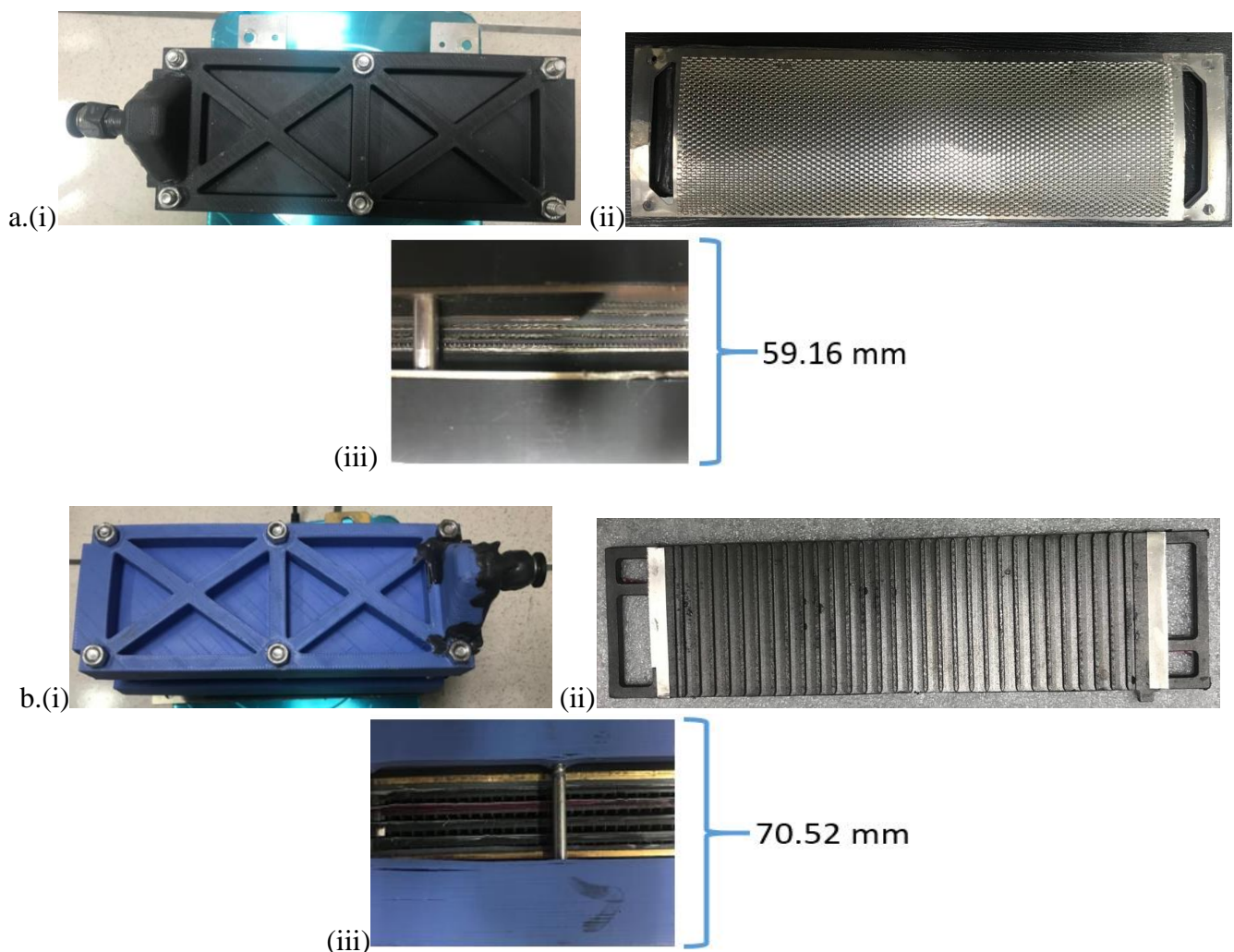

Figure 1. Comparison of metallic BP to graphite, a. (i) metallic cell stack, (ii) single metallic BP, (iii) side view of the metallic stack; b. (i) graphite cell stack, (ii) single graphite BP, (iii) side view of the graphite stack.

Figure (1), presents a stack of three cells; a. with metallic (titanium) BPs, and b. with graphite BPs. The stacks gave an overall thickness of 59.16 mm, with 1113.0 g, and 70.52 mm, with 1398.5 g respectively. This confirms that metallic bipolar plates come with increased overall volume, which further increase the total weight. Metallic BPs have properties such as reduced weight and size while maintaining low cost, high conductivity and mechanical strength. These properties are feasible through the adoption of microthin metal sheets. This further expands the application of cells to portable and dynamic systems.

3. COMMON METAL BP CHALLENGES

The main challenges in metallic plates are the fabrication process and corrosion. Thinning, rupture, warpage, spring back, and poor surface topography are common in fabrication. Corrosion is usually problematic during operation, mainly because of the operating conditions. This can be mitigated through coating, which is in trade with conductivity, unless a high-quality coating material is employed. This eventually hikes production costs. BPs designs come in different patterns. Traditionally, there are straight channels and serpentine channels. To attain even higher performance, the channels have to be improved with the developments listed in section 4. In all the designs, the main limiting factors are life span, performance, fabrication process and cost.

If the cost could be ignored, PEMFCs would be among the leading power density devices. Cost always compromises efficiency and lifespan. For example, the catalyst material (platinum) is expensive. Therefore, the catalyst layer should be well accounted for, to control cost.

The development of metallic BP brought the feasibility of fine mesh adoption. A fine mesh requires an extra conductive sheet to serve as a separator in a stack situation. Cost also limits the adoption of highly conductive materials.
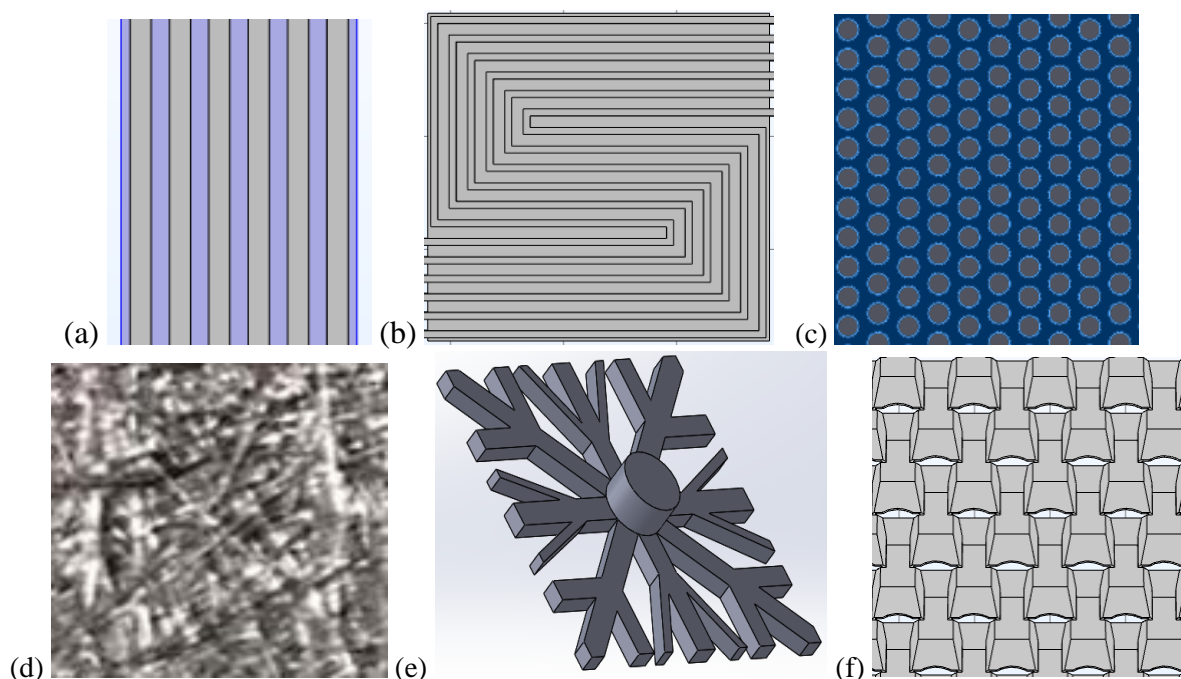
4. BPs DESIGN

BP design plays a prominent role in cell performance. It also limits the forming method. Figure (2) presents different designs recorded in literature [32]. These are conventional parallel channels, serpentine channels [33], interdigitated channels, metal foam filled channels [8,9], bioinspired channels [34], lattice patterns, pin types, and fine meshes [21,22,35]. The key factors governing BP design are even species distribution over the active area, good drainage of electrochemically generated water, enhanced positive diffusion of species, and negative diffusion of byproducts. The selected material should be a good conductor of both electricity and heat energy. Recently, channel constriction and fine mesh have drawn eminent interest because they are believed to enhance diffusion [21,36], which has to do with pressure drop. Agglomeration and delimitation are among the key cell degradation processes associated with enhanced diffusion. In serpentine channels, the nature of the bends plays a prominent role in the pressure drop [33]. With the channel cross-section, the diffusion rate is quite high along the channel edges over the axial flow direction. This region is believed to be dominated by low velocity due

to the double drag force exerted by the GDL and the channel wall. Numerous tiny channels and ribs have shown better performance than medium-sized channel rib patterns. In fine mesh BPs, the angle at which the plate leaves the GDL has predominantly significant effects on the diffusion rate. The region in front of the rib is dominated by negative water diffusion.

Foam-filled flow field: The foam-filled flow field has an eminent pressure drop and increased hydrophilic properties. With lengthy cells, it is recommended to only fill the foam half way from the inlet to the outlet. This is because as you go downstream, the electrochemically generated water increases. Foam is not recommended in this region because it delays water drainage, which might lead to flooding, thus negatively affecting the cell performance. Controlling the foam's internal structure is a challenge.

Fine mesh: A fine mesh has been noted for its 3D flow field, allowing even species distribution. The fine mesh has symmetric properties over the axial direction. Although it has positive performance, it has a high pressure drop, which demands fluid pumps to boost the flow. This increases the system's BOP. Fine mesh has a high product cost, which has compelled researchers to adopt the already existing wire mesh, as shown in Figure 2. (g) [37].

In addition to the flow pattern, the inlet is influential in active area utilization. It should be designed in a way that the reactants reach every part of the active area as soon as it enters the cell. No part of the cell should ever starve of reactants as this becomes a waste of material. Reactant-imbalanced cells are prone to stress, which accelerates their degradation. The outlet should also be well designed to ensure that all the generated fluids leave the cell. More attention should be directed to the corner regions of the flow field as the fluid turns to suffer vorticity. The design should generate forced convection compared to laminar flow. This enhances species diffusion through the GDL to the triple phase layer. Foam-filled channels and fine mesh have shown outstanding results because they impose forced convection.
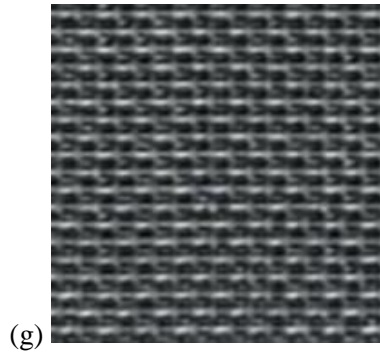

(a)   (b)   (c)

(d)   (e)   (f)

(g)

Figure 2. BP designs: (a) parallel channels, (b) serpentine channels, (c) pin-type plate, (d) foam filled in channels, (e) bioinspired channels, (f) fine mesh plate, (g) fine wire mesh.

5. BPs FABRICATION METHODS

Machining is the traditional BP fabrication method. This is more common with graphite due to its material characteristics. Graphite is too brittle to accommodate other fabricating methods that will call for bending or infliction of high pressure. In addition to brittleness, graphite is costlier and leaves high material waste during machining. In recent years, metallic BPs have opened up room for other fabrication methods, such as molding, stamping, high-velocity forming, extrusion, pressing, punching, hydroforming, hot metal gas forming [28], electromagnet forming [38-40], and many others, depending on the pattern complications. Metallic BPs further came with improved production rates. All these methods have their limiting factors. As previously mentioned, the application specifies the fabrication track. The lucrative automobile industry demands light weight, low volume, high power density, resistance to vibration failure, and durability. This will definitely demand thin sheet metals.

During fabrication, BP channel quality is solely dependent on sheet thickness, applied load, loading rate and dice velocity, dice outer corner radius, number of channels, draft angle, friction coefficient, and channel aspect ratio. Therefore, these need to be well scrutinized before fabrication is undertaken. Channel depths have been improved through the institution of soft stamping processes, hot forming processes, hydroforming and mold lubrication, and electromagnetic forming. It is worth nothing that different materials come with different spring-back values, so tolerance should be set according to the temperature and material.

5.1. Rigid die/Solid dies Pressing/stamping forming process:

This method requires a die that will be fashioned as per the flow field pattern. There should be a female and a male part. A load is applied to one part of the die while the other is held stationary, although it is also possible to have both dice loaded. Exerting the load on both the female and male parts has more advantages over the aforementioned method (it minimizes the chances of sheet failure). Sheet tearing is a common failure associated with the pressing method. Recent literature has recorded different types of dice apart from conventional hard metal dice. These are soft dies that include leather, spring packed,

wooden, and rubber. Soft dies are effective measures in mitigating plate failure during the pressing process. Sheet failure is more common over the bend region, which is susceptible to stress and strain (Figure 3), [41,42]. The soft dies inflict minimized stress and stain while compromising the sharp bends over the channels. Even if there is no literary failure (fracture) during pressing, the bend region remains the weak zone and is more vulnerable to failure during corrosion attack because stretching is more concentrated there if hard dies are used. The mechanical strength character is a limiting factor for material ductility. Considering cost, conductivity, mechanical strength and other properties, stainless steel is in the lead. The main challenges encountered by stainless steel are corrosion and limited ductility. Stainless steel, which is commonly used in thin metal sheets, has a high rate of bend (corner) failure.

An increment in channel width allows the plate to accommodate even deeper channels with fewer failure trends. This is recorded in reference [31], where material formability was compared. SS304 surpassed all the other materials, and AL 3104 appeared to be the least capable material. In almost all the studies recorded in literature, the transverse direction channel filling percentage and thinning percentage are not the same as those of the longitudinal direction. If not well monitored, this feature greatly affects the quality of the cell, as the GDL-BP contact pressure varies according to the channel depth on assembly. This creates stress in the active region as the rib compresses the GDL, thus closing its pores. It is not easy to attain even filling percentages and even thinning percentages because they are dependent on each other. Thinning is more severe over the channel walls and outer corners than in the channel base (Figure 3). An alternative to mitigate thinning of the metal sheet during forming is using flexible dies with polymer powder medium-PVC powder (polyvinyl chloride powder) [43], which allows the die to pull the metal sheet to the fashioned channels with less stretching and thinning. When only rigid dies without powder are used, wrinkles and contorts are created in the channel-free region. This is due to compression created by pulling over the die curvatures. In the former method, the powder holds the sheet flat, with the forming temperatures still high; this allows the metal sheet to remain in the flat position even after load removal.

The sheet thinning percentage is calculated as [44]:

- $Thinning \% = \left(\frac{t_o - t_f}{t_o}\right) X\ 100$ (1)

Where t_0 and t_f are the original sheet and final sheet thicknesses, respectively.

The filling percentage of the sheet (S_{total}) [28]:

- $S_{Total} = \frac{\int f(w_s, R_s, r_s, h_s)}{\int g(x)} X100$ (2)

Where w_s = channel width, R_s= formed outer corner radius, and h_s= formed sheet maximum height, $r_{s,}$= formed inner corner radius, $g(x)$ = groove area with a specified dimension.

Uniformity error can be depicted by equation (3)

- $e_u = \left(\frac{h_k - h_m}{h_m}\right) X\ 100$ (3)

Where e_u= uniformity error, h_m= maximum channel depth, and h_m = minimum channel depth.
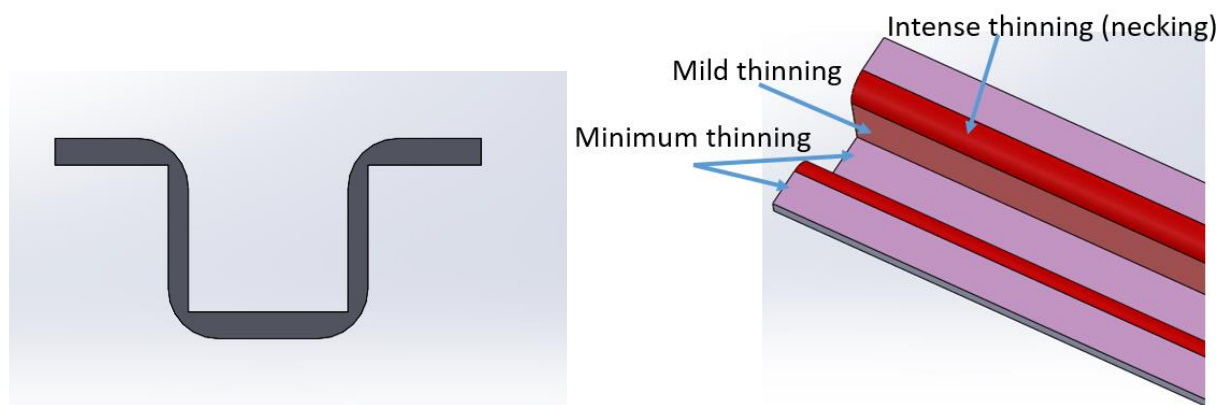
Figure 3. Metal sheet thinning distribution over the channel.

5.2. Rubber pad (RP) forming process

In an effort to eradicate failure in BP fabrication, researchers have invented concave channels [45], and RP forming process. The effects of metallic BP forming RP have been recorded in literature [46,47], and it was determined that the rubber hardness, thickness and loading rate are crucial parameters. The rubber had to be machined in the same pattern as the desired flow field and then fitted to a solid metal holder. A metallic top die with an alternating pattern to that of the rubber has to be attached to the press moving part to serve as the male part. With reduced rubber hardness, increasing the rubber thickness and load force produces deep channels. In conclusion, the metal sheet stretches more over the die outer bends because of the high force concentration. A prefolded metal sheet to cater for the bends stretching can be set as a novel idea for future work. This idea is more feasible in straight channels. Improving both the rubber and the die surface texture has significant contributions to mitigating sheet fracture during pressing. Channel depth is also dependent on the channel nature and spacing. The more channels there are, the shallower the depth, and the opposite applies to fewer channels. Forcing the depth results in fracture because of excessive sheet stretching. RPs attenuate stretching from being concentrated in one region, thus alleviating rupture. The inability to control the pressure distribution on the RP is one of the major drawbacks that causes uneven thickness over the formed plate [28]. It is important to maintain a homogenous channel depth to ensure uniform GDL-BP contact and compression pressure on cell assembly. Therefore, RP-forming stages have to be integrated with that of solid dice for improved finishing. Necking is the common initial sign of failure during metallic BP fabrication [47-49]. The die outer corners and surface finish have a significant contribution to metal sheet failure. Sheet morphology is crucial in BP forming. Rough surface plates result in quick tearing during pressure load application. An optimum outer corner radius of 0.4 mm under a draft angle of 40° and a 0.05 friction coefficient have been recorded [47]. Increasing the corner radius reduces the intensity of necking over critical regions as the strain is shared over a vast area. Increasing the outer corner radius from 0.1 to 0.4 mm improved the critical region by 0.15 mm. In contrast, for a 100% rubber filling effect, a 0.2 mm corner radius,15° draft angle and 1.6 ratio have been recorded as optimal [50]. A 0.2 mm corner radius has been adopted by a number of researchers [50-45] as the optimum value.

Considering BP multifunctions, it is worth mentioning that the corner radius increment has negative effects on the BP quality, which plays a conspicuous role in reactant distribution, pressure drop, current density, and cell performance as a whole. This negativity is not only applicable during the forming process; sharp corners increase the fluid flow drag force, while blunt corners reduce the BP-GDL contact surface area. Machined RP increases the fill in amount and shares the strain over a wider area than being localized. These increase the formed channel depth. For the boundary conditions, elastic–plastic material can be assigned to the SS316 L plain metal sheet, and hyperelastic material model can be assigned to the polyurethane RP for the numerical analysis, which corresponds to the experimental analysis. A high von Mises stress and effective plastic strain should be recorded in the corner regions. This confirms the metal sheet's nonuniform thickness after fabrication. Die velocity also plays a prominent role in rupturing probability [46]. In addition to plate failure, the RP corners are also susceptible to failure. Therefore, it has to be strictly monitored. Plate and die lubrication is important during metallic BP fabrication. It improves the filling ratio to approximately 83% [51]. Variation in the stress state can be used to evaluate the capacity of ductile fracture criteria during metallic BP RP forming [50]. Ayada, RiceTracey, and normalized Cockroft-Latham have to be used in this prediction. Equation (4-6) is adopted to numerically portray ductile measures [50]:

$$D_1 = \int \frac{\sigma_m}{\bar{\sigma}} d\bar{\varepsilon}_p = \int_0^{\bar{\varepsilon}_p} \eta d\bar{\varepsilon}_p \tag{4}$$

$$D_2 = \int_0^{\bar{\varepsilon}_p} \exp\left(\frac{1.5\,\sigma_m}{\bar{\sigma}}\right) d\bar{\varepsilon}_p = \int_0^{\bar{\varepsilon}_p} exp(1.5\eta) d\bar{\varepsilon}_p \tag{5}$$

$$D_3 = \int_0^{\bar{\varepsilon}_p} exp\left(\frac{\sigma_{max}}{\bar{\sigma}}\right) d\bar{\varepsilon}_p = \int_0^{\bar{\varepsilon}_p} \left(\eta + \frac{2\left(cos\frac{\pi}{6}(1-\bar{\theta})\right)}{3}\right) d\bar{\varepsilon}_p \tag{6}$$

Where $\boldsymbol{D_i}$ represents the critical damage parameter for each criterion, which is the integration of the weight function until the fracture strain $\bar{\varepsilon}_f^p$ $\left(\bar{\varepsilon}_p = \bar{\varepsilon}_f^p\right)$. At damage value critical point, damage begins. Therefore, the stress state history is crucial in ductile fracture criteria calibration. Table 1 lists some of the materials that have been tried, along with their forming process.

5.3. Hot metal gas forming process

Engineers and scientists have developed several approaches to attain more effective BP forming processes, which are also cost effective. The hot gas forming process [28,54], which is a high power density innovation, has been recorded with favorable qualities. Hot metal gas forming involves heating the metal sheet to high temperatures to increase its ductility. High ductile metals can sustain high stretching with reduced rupture chances. High-pressure gas (argon) is then blown on the sheet side, thus allowing it to fill the die's curvatures, making a thin wall over it. The gas region should be airtight to prevent gaseous escape. This method is believed to have reduced necking as stretching is distributed all over the channel region. Unlike other methods, which turn out to have pronounced thinning over the corner regions. Although this process has high quantity production compared to graphite machining, it is still considered time consuming compared to traditional stamping. Hot metal gas forming has high capital and running costs. The high operating temperatures complicate blown-in air sealing. In addition to sealing challenges, annealing reduces the mechanical strength of the material, which affects the PEMFC compression pressure. As a result, the ICR becomes higher. Because of the sheet

microthickness, mechanical strength loss is irreversible. Reference [28] revealed hot metal gas forming optimum operating conditions of temperature 400 °C, gas pressure 40 bar, channel wall angle of 7.5°. Increasing the channel angle allows an even higher fill-up ratio, although it compromises the BP quality. The aspect ratio is massively influential in channel formability. A higher aspect ratio results in a high fill-up percentage and high production rates [54]. Thinning increases with increasing aspect ratio, while it decreases with increasing outer fillet radius. The hot metal gas forming process recorded an optimum outer fillet radius of 0.2 mm. Further increasing this radius ruins the BP quality, as it means there will be a high rib surface area, leading to poor reactant supply. It is worth noting that hot metal gas forming is highly effective in ductile materials. In the hot gas forming process, using a blank with variable thickness lightens the weight of the formed part compared with a constant thickness blank [55].

Table 1. BPs forming process

Forming process	Material	Channel depth (mm)	Channel Width (mm)	Channel type	Sheet thickness (mm)	Reference
Stamping	SS 304	≥0.36 &≤ 0.54	1.2 & 1.8	serpentine	0.1	[31]
Stamping	SS 316 L	0.68-0.72 & 0.63-0.65	1,0.89	serpentine	0.1	[51,24]
Stamping	Titanium - Grade2 (CP-Ti)	≤0.36 & <0.54	1.2 & 1.8	serpentine	0.1	[31]
Stamping	Aluminum (Al 6016)	≤0.36 & ≤0.54	1.2 & 1.8	serpentine	0.1	[31]
Rubber forming	Titanium	≤0.270	0.8	serpentine	0.1	[53]
Stamping	Aluminum (Al 3104)	<0.36 & <0.54	1.2 & 1.8	serpentine	0.1	[31]
Soft die forming (leather, rubber, spring)	SS 316	≤0.70	1.1	serpentine	0.1	[45]
Electromagnet forming	2024-T3 aluminum alloy				1.2	[56]
Hydroforming	(SUS304)	≤0.73		Parallel	0.1	[57,58]
Hot metal gas forming	AA1070	≤0.57	1.2	parallel pattern	0.1	[28]
Stamping	titanium alloy	≤0.4	0.42	Fine mesh	0.05	[20]
PPFF	C1100	≤0.6	0.9	serpentine	0.1	[43]
roll forming (bending)	SS304 L	≤0.4	0.58	parallel	0.1	[44]
rubber forming	titanium	≤0.27	0.8	serpentine	0.1	[52]

6. BPs COATING

BP coating is a significant approach in mitigating corrosion, ICR and heat resistance, which are prominent drawbacks in fuel cell development, depending on the substrate material. Conduction properties should never be ignored, as the substrate's major property should only be entrusted to the coating. This is because the coating only serves as a conduction intermediator between the substrate and the GDL. If conduction can be fully assigned to the coating, high resistance will result because the current will have to travel over a thin cross-sectional area. Corrosion has three main effects on cell quality. 1. It poisons the cell MEA. 2. It deteriorates the cell contact surface, thus increasing the ICR. 3. Reduces cell mechanical stability as the plate disintegrates. Resistance inflicted by oxide film and charge transfer is prominent in the overall cell impedance [59]. Numerous developments to mitigate this resistance involve the use of high-quality materials, such as gold, silver, copper, alloyed materials, and coatings. As cost reduction is among the major concerns in this development, it is noted that under small-scale production, only coatings can effectively address the aforementioned drawbacks. Coating mainly improves the BP conductivity, resistivity to corrosion and dissolution, but sometimes the two properties have to compromise due to cost as the limiting factor. Using the coating material (gold, silver, etc.) as the BP base (only material) would dramatically escalate costs. Additionally, some of these materials cannot stand alone with microthickness due to mechanical strength and chemical stability; therefore, they can only serve as coatings. Different BP coating methods are recorded in the literature, and some are still under development. These include physical vapor deposition (PVD), electroplating, airbrushing sputtering, and cathode arc ion plating, as listed in reference [60] and Table 2.

Table 2. BP coating methods

Coating method	Coating material	Base material	ICR ($m\Omega\ cm^2$)	load ($N\ cm^{-2}$)	Reference
High-energy microarc alloying	Titanium diboride (TiB$_2$)	SS304	19	150	[61]
Electrodeposition (cyclic voltammetry)	polypyrrole/graphene composite	SS304	20	150	[62]
direct current and pulse magnetron sputtering	Ti$_3$SiC$_2$	SS304	10	150	[63]
chemical vapor deposition	Tantalum	SS316 L coupons	22.3e32.6	140	[64]
direct current (DC) magnetron sputtering	amorphous Al-Cr-Mo-N	SS316 L	32.5 ± 0.5 (anode) and 34 ± 0.55 (cathode)	150	[65]

hydrothermal and impregnation process	carbon/PTFE/TiN composite	Ti	13	160	[66]
electrodeposition	polypyrrole-graphene oxide/polypyrrole-camphorsulfonic acid bilayer (PPY-GO/PPY-CSA) composite	SS304	16.7		[59]
pulse electrodeposition	Ni and Ni-Cr-P	AISI 1020 low-carbon steel	49.1	150	[67]
reactive magnetron sputtering	chromium nitride	SS316 L	8.4	150	[68]
disproportionation reaction	β-Nb2N	AISI 430 FSS	5.2	150	[69]
electrophoretic deposition (EPD) technique	hydrophobic G-ODA-TiO$_2$	copper	9	150	[70]
	G-TiO$_2$		10.2		
thermal spray {High velocity oxy-fuel (HVOF)}	NiCr	aluminum	38	150	[71]
	NiCrBSi		17		
	(Co,Ni)CrAlY		108		
insitu electrodeposite	PPY-GO composite	SS304			[72]
electrodeposited galvanostatically	TNO-PANI composite	SS316			[73]
	PANI				
Plasma Enhanced Chemical Vapor Deposition (PECVD) method	diamond-like carbon (DLC) film	SS316	2.0 – 22.3		[74]
	hydrophobic Polytetrafluoroethylene (PTFE)/Carbon cloth/Ag multilayer	Magnesium alloy (Mg)	27.28	140	[75]
close-field unbalanced magnetron sputtering ion plating (CFUBMSIP)	Carbon with small amount of tungsten($C_{W0.2(A)}$)	SS316 L	6.25	150	[76]

6.1. Coat selection

In addition to corrosion resistance and conductivity, numerous other qualities are considered in BP coating materials and method selection. These include thermal expansion, lower ionic contamination toward metal plates, adhering strength, inertness, solubility under extreme conditions, and lower density and volume. Through these qualities, it is irrefutable that not every coating material can be applied to any base metal. CrN and TiN were applied on SS316 L surfaces through cathode arc ion plating (CAIP), and 100 mΩ cm^2 and 113 mΩ cm^2 ICR decreases were obtained in CrN and Tin coatings, respectively [77]. CrN and TiN lowered the corrosion resistance by 9.9 μA cm^{-2} and 9 μA cm^{-2} respectively. This study has proven beyond doubt that CrN-coated 316 L BP renders optimum qualities. Many coatings recorded in literature already qualify 2020 DOE targets. Titanium dibromide (TiB_2) can be used to coat stainless steel 304 through a high-energy microarc alloying process [61]. Under a 150 Ncm^{-2} load, the TiB_2-coated 304SS plate gives an ICR of 19 mΩ cm2, which is far below that of the bare plate. The TiB_2-coated substrate recorded 3-4 orders of corrosion resistance, which was higher than that of the uncoated substrate. This material is cost effective. The main challenges associated with TiB_2 lie with its high melting point, making it not adaptive to common coating techniques. The cross-sectional morphology of the TiB_2 coating presented in [61] shows separation between the foremost top surface and the underlying layer. This might be attributed to residual stress resulting from a temperature gradient on cooling. The cooling gradient is a critical factor in high-energy microarc alloying techniques. These phenomena will definitely hike contact resistance. In the literature, steel has been coated with TiB_2 through other techniques [78,79], mainly to improve the tribological behaviors of steel surfaces. Researchers [53] experimentally proved titanium hardness and ICR improvement after coating it with TiN. Coating is influential not only on metallic BP but also on graphite. *The* PVD technique has been used to coat composite graphite with PTFE and SiO_2, obtaining contact angles of 120.2º and 35º respectively [80]. This proved to be a drastic improvement in performance compared to uncoated graphite. Metal carbides have also been recorded as suitable coating materials for some substrates [81-83]. In addition to the base material, the coating technique and materials are also governed by the type of flow field pattern, which further determines whether the coating should be applied prior or after the forming process. This is because, for the coating to be effective, it should come with no defects, such as pinholes, poor morphology, dents, etc. Corrosion and decay can propagate under the coating, reducing cell performance. It is crucial to maintain a minimum possible coating thickness to maintain a low volume size and weight. Grazing incidence X-ray diffraction (GIXRD) analysis can be used to determine the phase composition of thin coat films [76].

6.2. Conductivity behavior

Both the coat and substrate should have good conduction properties. As mentioned above, if conduction can be fully assigned to a coating, high ohmic resistance will result because the current will have to travel over long and thin longitudinal directions. The current passing through a media depends on the number of electrons through the media's cross-section per unit time [84,85]. Therefore, the larger

the cross-sectional area is, the more electrons can pass per unit time. This is portrayed by Pouillet's law, Equa. (7):

$$R \propto \frac{L}{A} \Rightarrow R = \rho \frac{L}{A} \qquad (7)$$

Where R is the resistance, L is the conductor length, A is the conductor area, and ρ is the conductor resistivity.

Incorporating the influence of temperature, equation (7) transforms to equation (8) [86]:

$$\frac{dR}{dT} = \frac{d}{dT}\left(\frac{\rho L}{A}\right) = \frac{d\rho}{dT}\frac{L}{A} + \frac{dL}{dT}\frac{\rho}{A} - \frac{dA}{dT}\frac{\rho L}{A^2} \qquad (8)$$

Where T is temperature. It is worth nothing that the term *(dρ/dT) (L/A)* denotes the resistance change because of the temperature dependence of the resistivity of the conductor, and *(dL/dt) (ρ/A)-(dA/dt) (ρL/A^2)* denotes the influence of thermal expansion.

Carbon and metal carbides are commonly adopted coating materials, although they have some defects [87]. Carbon has been recorded for its significant conductivity and reduced cost. Carbon has to be combined with other elements to improve its corrosion resistance and adhesion strength. Adding PPy and PDA can enrich the carbon coating properties. Adding only PPy to carbon (PPy/C) improves corrosion efficacy to 93.03%, and adding PPy and PDA (PPy/C-PDA) renders 98% improvement [14].

6.3. Wettability

In addition to the already stated BP properties, wettability is a critical property that needs to be accounted for. The BP morphology is the main attribute to fluid flow efficiency. A poor surface morphology significantly contributes to the fluid drag force, resulting in poor byproduct drainage. The hydrophobic and hydrophilic properties of the coating materials should be well analyzed to understand their wettability. An increased drag force on the channel periphery can further result in a hydrophilic surge, which turns out to spoil the coating quality. A quality-coated substrate should be of high hydrophobicity. A limited hydrophilic content is expected in the GDL to keep the cell well hydrated. Carbon cloth/Ag, Ag paste and PTFE/carbon cloth/Ag have condensed fluid contact angles of 130.3º 83.2º, and 141.8º, respectively [75], which shows that the latter has good liquid repelling properties. Isosurfaces can be used to visualize liquid behavior in fine mesh BP [21]. Equation (9) portrays the surface tension force resisting liquid droplet movement.

$$F_\sigma = \pi \sigma D \sin^2 \theta_i \sin \theta_H / 2 \qquad (9)$$

Where θ_H is the contact surface angle hysteresis. The gravitational effect is negligible because of the small Bond number. H is the flow field height, σ is the surface tension coefficient, and D is the droplet size diameter.

6.4. Carbon based Coating materials

Carbon and its compounds are promising coating materials for BPs [14,59,62,63,66,74-76,88,89]. This is attributed to their unrefuted good conductivity, corrosion resistance, chemical stability, and cost effectiveness. This is why it has been adopted as PEMFC BP in the form of graphite. Most of the previously mentioned qualities of carbon have already reached the DOE target. The main challenge

faced by pure carbon is its poor hydrophobicity and adhesion properties. Carbon alone has a smaller longitudinal coefficient of thermal expansion, which makes it prone to rupture when coating a substrate with a high longitudinal coefficient of thermal expansion under frequent temperature changes. These require an extra element or compound to improve these properties.

Diamond-like carbon (DLC) coating passes the ASTM D 3359 Test Method when four-point probe equipment (Signatone-PRO 4 with Keithley sourcemeter (model 2400)) is used to measure the electrical resistivity [74]. DLC films produced with CH_4 as a precursor gas exhibit outstanding results when applied to SS316 substrates through the plasma-enhanced chemical vapor deposition technique. When a lower power (approximately 250 W) is used during coating, argon gas should be added, as this drastically increases the sp^2 bonds and improves corrosion resistance and hydrophobicity. Carbon/PTFE/TiN composites have been used for titanium through hydrothermal and impregnation processes [66]. Hydrophobic polytetrafluoroethylene (PTFE)/carbon cloth/Ag multilayers have been used for coating Mg alloys, and they lowered the ICR (at 140 Ncm^{-2}) and corrosion current density by 72.9% and 99.6%, respectively [75]. Although the stated properties were acceptable, their approach still came with a slightly higher coating thickness of 450 μm. Carbon-coated SS-316 L and AA- 6061 substrates, through direct current magnetron sputtering physical vapor deposition (PVD) at 7x10-6 bar, are presented in reference [88]. To enhance adhesion, the substrates were heated to 100 °C prior to deposition. This was followed by cooling to room temperature in the sputtering chamber upon completion of deposition. Carbon coating is effective within a limited thickness range in SS316 L, with an optimum thickness of approximately 200 nm. AA-6061 showed a positive response as the carbon thickness was increased from 100 to 600 nm, although the results were far lower than those of the SS316 L substrate. These results do not satisfy DOE's 2020 and 2025 targets. An increase in coating thickness weakens the adhesion strength, making the substrate more susceptible to corrosion. Coating SS-304 BP with an improved conducting polypyrrole anti-corrosion coating containing functionalized carbon powders through polydopamine (PDA) is proposed in reference [14]. Numerous studies have used *X* M H_2SO_4 to simulate fuel cell operating conditions [75,76,88,89]. The diamond-like carbon (DLC) film used to coat the SS316 substrate recorded a minimum ICR of 2.0 mΩ cm^2 (Table 2).

(ii)

Many studies [14,75, 90-92] have adopted *Davies's approach* [93] in measuring the ICR of coated BP (Figure 4), and the contact resistance can be portrayed through equation 10 [93]:

$$R = \frac{VA_s}{I} \tag{10}$$

Where R is the electrical contact resistance, *V* is the voltage across the metal sample, *I* is the applied current, and A_s is the contact surface area. The load pressure is varied to obtain the optimum value, although it should comply with the cell operation load pressure.

Special attention should be given to carbon coatings because nanosized carbon particles possess strong Van der Waals forces toward each other, which result in agglomeration. This was well demonstrated in reference [14] supplementary file. A dispersant should be added to the coating method. Agglomeration of the carbon particles results in poor conduction paths.

SS316 L can be effectively coated with tungsten-doped carbon film. A close-field unbalanced magnetron sputtering ion plating (CFUBMSIP) coating system equipped with one chromium target, one tungsten target, and two graphite targets has been used to deposit carbon films [76]. The smaller

[W0.2(A)] amount of tungsten improves corrosion resistance and self-passivation. A small increase in ICR values stems from microstructural changes in the carbon film imposed by different tungsten concentrations.
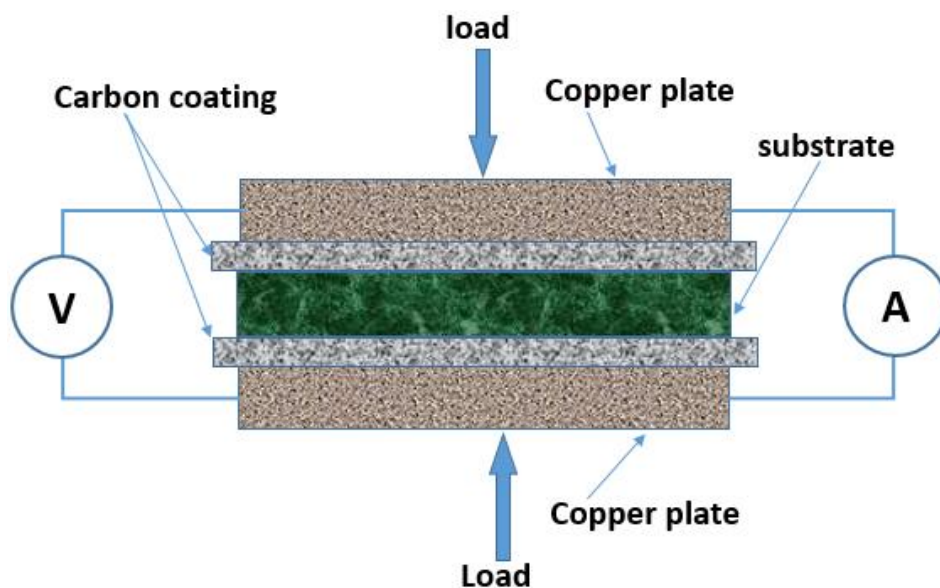

Figure 4. Interfacial Contact resistance assembly's schematic diagram

6.5. Coating Adhesion Test

The coat quality should satisfy adhesion, morphology, electrochemical corrosion, electrical resistivity, wettability, and structure tests. Coating strength can be scrutinized using different tests, including the ASTM D 3359 Tape test, scrape adhesion test, pull-off test, and cross-cut test. The ASTM D 3359 method can be split into two categories, one for coating thicknesses under 125 μm and the other for coating thicknesses over 125 μm [94]. In performing this test, a hard, sharp object is used to scribe a specified pattern on the surface of the coated substrate. A cross-cut lattice pattern is preferred for less than 125 μm, while an X-cut is preferred for more than 125 μm, with a leg of 38.1 mm. For the X-cut, a 30-45° intersection angle is recommended. For 50-125 μm, six incisions spaced at 2 mm are recommended, while for less than 50 μm coating thickness, 11 incisions spaced at 1 mm are optimum. A pressure-sensitive tape conforming to ASTM D3359 standard, is applied to the scribed pattern and rapidly pulled as shown in Figure 5. The debris picked up by the tape is evaluated based on the ASTM standard to judge the coating adhesion strength. Sometimes the test results will have to be assessed under a powerful microscope. A pull-off test adhesion testing method has been adopted on Mg substrates coated by three different materials (PTFE/carbon cloth/Ag, carbon cloth/Ag, and Ag paste) [75]. The adhesion strength results revealed that PTFE/carbon cloth/Ag, carbon cloth/Ag, and Ag paste coatings have a strength of 2.88 MPa, 4.34 MPa and 4.95 MPa, respectively. This method has also been applied to test the adhesion strength of functionalized carbon powder on SS304 BP [14].
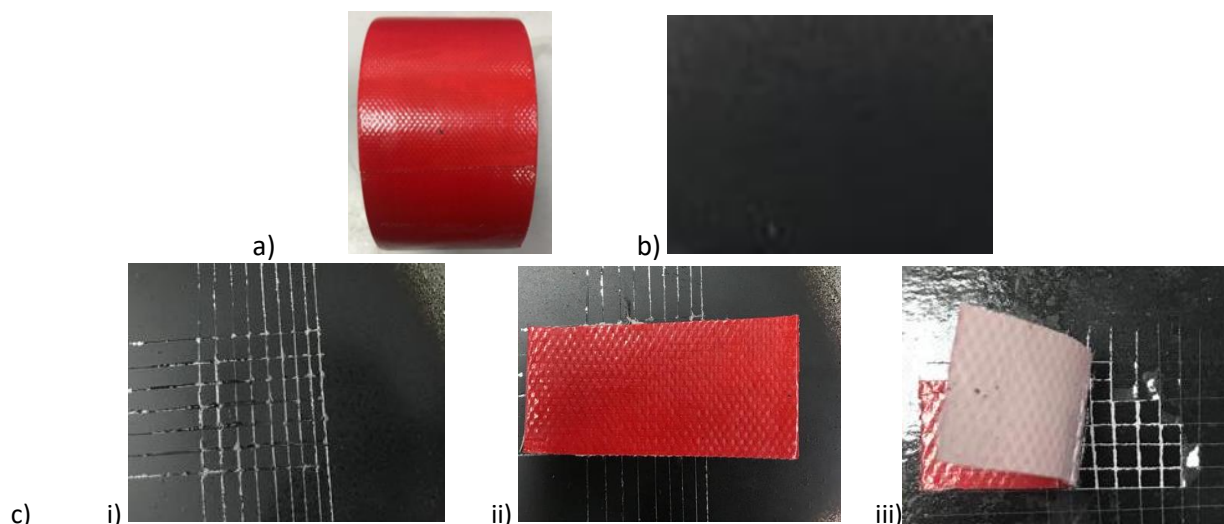
Figure 5. Adhesion test using Cross Hatch Tape and the procedure, a) tape, coated substrate, c) testing procedure

7. PROPOSED STUDY TO MITIGATE METALLIC BPs FAILURE ON FABRICATION

The fuel cell fraternity has already met most of the targets set by the DOE, [95,96], although there are still some to be addressed. In this section, we propose a novel hybrid roller forming and stamping process to mitigate the fabrication challenges by approximately 80%. In all the recorded studies, thinning seems to be the critical criterion that leads to rupture in metallic BP formation. Among metallic BP fabrication methods, the microroll forming process is less prone to this challenge [44,97-100], but it is expensive and more conducive to only large channel sizes. Microroll forming has recorded a minimum thinning of 25% [44]. In traditional stamping, quantity production resulting from a high production rate due to simplicity leads to a low production cost. Stamping is usually carried out in multiple stages, which helps mitigate sheet thinning [101]; this evenly distributes the stretching force rather than concentrating it in one location, thus lessening the necking intensity [23]. The proposal presented in this section is almost the same as the tube wringer process, which is commonly used in honeycomb microchannels and has been noted to be less affected by thinning [102].
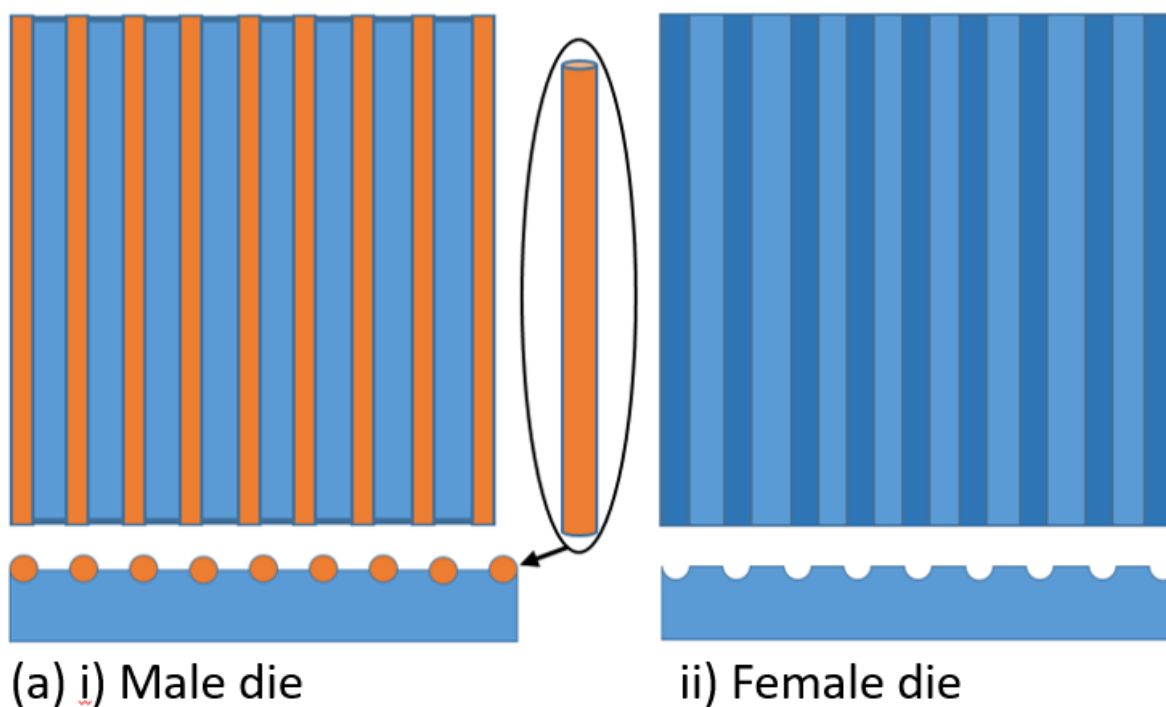
Through the ideas acquired from this review, a hybrid integrating roller pressing and stamping technique is proposed. The proposed novel method comprises two phases, the initial and final phases, with two steps in each phase. The initial phase solemnly constitutes roller-furnished dice (Figure 6 (a) and 7(a)), while the final phase constitutes rigid dice (Figure 7 (b) and 11(b)). This novel idea is targeted to mitigate thinning- and necking-related failure. The rollers mounted in the die will allow the thin metal sheet to be pulled and engraved according to the desired pattern with reduced tension stress, thus resulting in no/less thinning.

First phase: The first step roller die should have a slightly smaller (almost half) rib (male tooth) width to that of the channel (female engravings) compared to the second die, although the female engraving should be the same in width for both the first and second rollers. The first phase channel depth should be slightly deeper than that of the final phase. This allows the sheet to be compressed when taking

the final shape (mainly when taking the corner shape) rather than being stretched [44]. Additionally, it should be noted that to avoid necking in the corners, the first phase step does not have sharp corners, as only rollers are used.

Second phase: The second phase steps have corners that become more pronounced as you approach the final stage. The second phase stamping should also be in the same order as the roller dies, although the male die width should be the exact final channel geometry. The only difference between the two final phase dice geometries is the corner dimension. It should be noted that the final pressing stage has pronounced stretching compared to all the other stages. Any undesired deformation created during roller pressing is fixed on rigid pressing. To maximize the efficiency of this state-of-the-art forming technology, the whole process should be performed while completely immersed in a lubricant. Lubricants have proven to be an effective medium in minimizing failure in metallic BP forming [51]. The load application should be in series to give a pulling vector and ensure that every part is lubricated; otherwise, the rollers will be less effective. The rigid die should be evenly loaded at once. Although each stage roller is identical, they have to be fitted into the die channels, one at a time. This allows the metal sheet to be drawn from one direction with minimal thinning or without thinning. After each roller fitting, the die is loaded. The already fitted roller is not removed to ensure that the already fashioned part of the plate does not stretch back and deform. This process will be time consuming compared to the traditional pressing process but effective.

The proposed stamping method is applicable to both straight channels and lattice patterns. For the lattice pattern, the rollers should be ball rollers (ball shaped) (Figure 7(b)) or needle bearings, inconsideration of the final pattern shape.
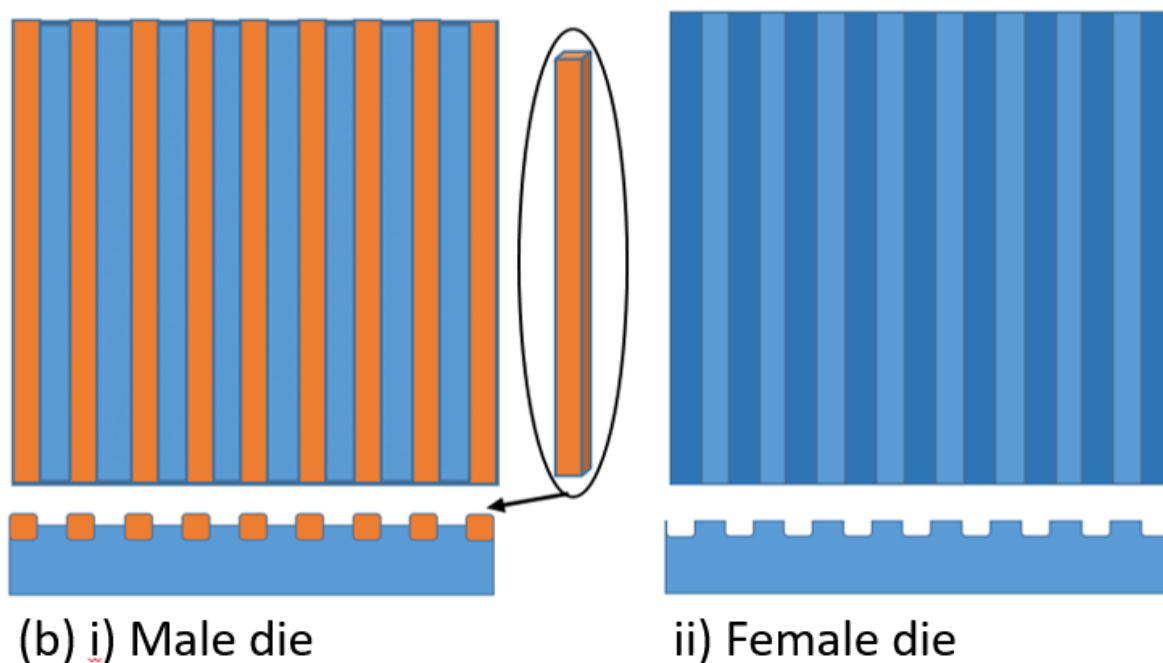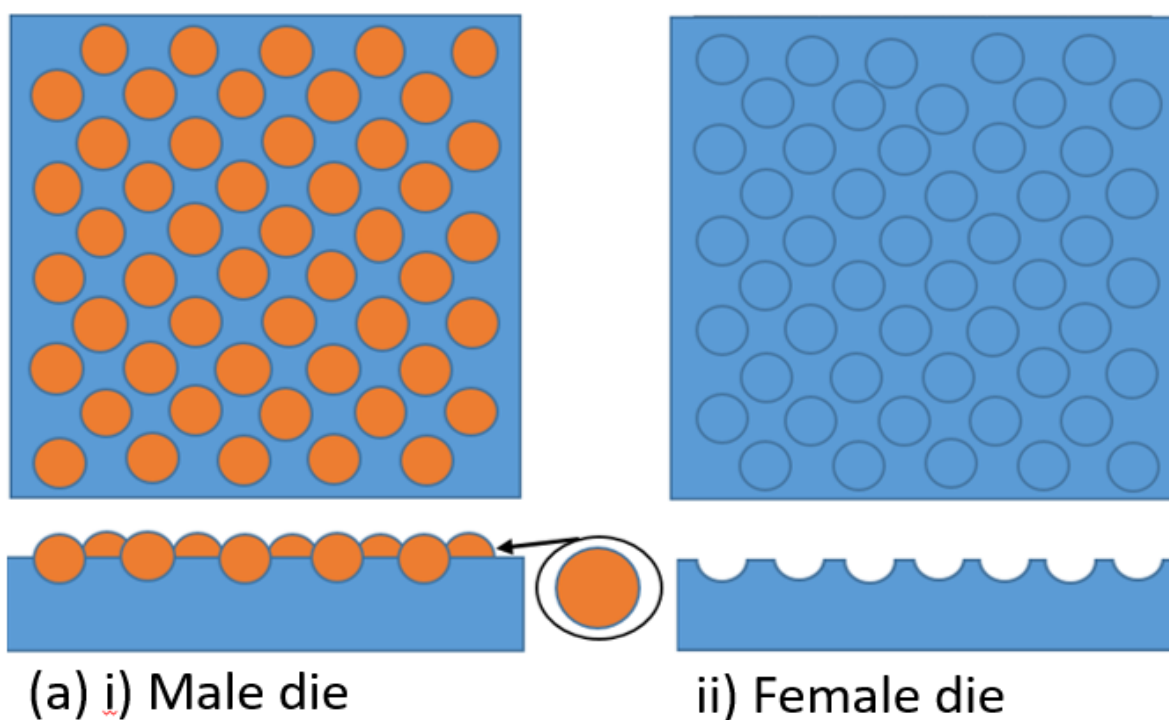

(a) i) Male die   ii) Female die

Figure 6. Straight channel schematic: (a) first phase pin roller die and (b) second phase rigid die.

Moreover, this forming technique is also favorable for already coated substrated dents, as it reduces friction and stress to cause dents. It is assumed to reduce thinning by approximately 80%. It is presumed that this technology is free from the misalignment challenges encountered in microroll forming with plates fed in axial movement [44]. This is because in this proposal, the plate has less axial movement. Slippage is beneficial because it ensures that thinning is not localized.
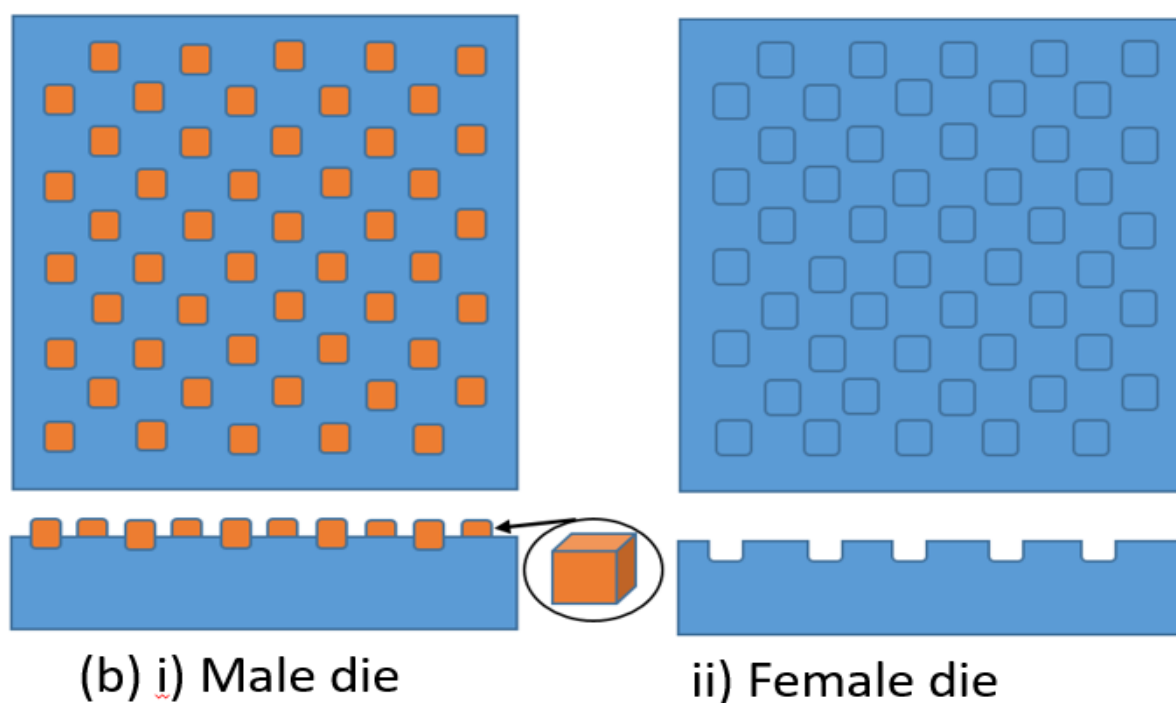
Figure 7. Pin pattern BP schematic, (a) first phase ball roller die, and (b) second phase rigid die.

7.1. Possible failure

This novel idea also has some possible challenges that can lead to failure, although they can be overcome with skill and careful attention. Miss alignment can be brought about by an extra hard foreign material than anticipated, which might bend the metal sheet or the rollers. Another possible failure may be brought about by wearing out of the bracket, the roller, or the female die, which may result in high friction between the plate and the roller. Pronounced thinning is anticipated toward the final stage of this forming process. This is due to the force exerted at the corners of the channels, although that thinning is not intense compared to the other forming processes revealed in literature. The outer region without channels is more prone to warpage because of strain accumulation from the force exerted in the last channel region. Under normal pressing, more load is applied in the corners of the die in almost all the stages. In this novel approach, over the first phase steps, the maximum load is concentrated in the central part of the channel as the rollers are cylindrical. Over the last stages, this region regains its thickness because it only experiences compression force.

To our knowledge, we are the first team to propose the invention of this hybrid technology in PEMFC metallic BP forming. It is believed that this approach will play a prominent role in improving production quality and reducing wastage due to failure and cost management because of the drastically reduced running costs. The reduced friction will dramatically reduce sheet rupture.

8. CONCLUSION

In this paper, we review the feasibility of metallic BP development and application to PEMFCs. Metallic BP has numerous outstanding properties that have been attributed to its application in dynamic

scenarios, e.g., automobiles and UAVs. They are effective in weight, volume reduction, high production rate, acceptable conductivity, tolerance to complicated design fabrication, and surface improvement feasibility. Their complications are corrosion, chemical instability under cell operation conditions, high thermal expansion, and high specific weight. Some carbon-coated metallic BP properties have reached some of the 2020 DOE targets. Some have even hit the 2025 target. Carbon is a great material to be adopted as a coating because it has good electrical and thermal conductivity, corrosion resistance, and chemical stability. It is further recommended for its reasonable price. Although carbon comes with so many good properties, it has poor adhesion properties; therefore, it has to be mixed with a bonding media, although it turns out to compromise the good qualities. Substrates coated with carbon-containing compounds recorded a minimum ICR of 2 mΩ cm^2. Carbon has acceptable hydrophobic properties. Coating not only improves cell performance but also its durability. During BP fabrication, failure is predominant in the outer curves of the plate because that is where the exerted force is more concentrated. The coating adhesion test is an effective and affordable approach for evaluating the coating adhesion strength. The proposed novel hybrid roller forming and stamping process is assumed to mitigate thinning by approximately 80%. This is because it comes with reducer friction and stretching. The novel approach is suitable for both straight channels and lattice patterns.

Reference

1. F.B. Weng, M.M. Dlamini, G.B. Jung and C.X. Lian, *International Journal of Hydrogen Energy*, *45* (2020) 12170.
2. S. Dey, and N.S. Mehta, *Resources, Environment and Sustainability,* (2020) 100006.
3. T. Wilberforce, Z. El-Hassan, F.N. Khatib, A. Al Makky, A. Baroutaji, J.G. Carton, and A.G. Olabi, *International Journal of Hydrogen Energy*, 42(2017),25695.
4. C.Y. Hsieh, P. Pei, Q. Bai, A. Su, F.B. Weng, and C.Y. Lee, *Energy*, 214 (2021) 118941.
5. H. Tsuchiya, and O., Kobayashi, *International Journal of Hydrogen Energy*, 29 (2004) 985.
6. R. Taherian, *J. Power Sources,* 265 (2014) 370.
7. Y.J. Ren, M.R. Anisur, W. Qiu, J.J. He, S. Al-Saadi, and R.S. Raman, *J. Power Sources,* 362 (2017) 366.

8.   B.T. Tsai, C.J. Tseng, Z.S. Liu, C.H. Wang, C.I. Lee, C.C. Yang, and S.K. Lo, *International Journal of Hydrogen Energy,* 37(2012) 13060.
9.   C.J. Tseng, B.T. Tsai, Z.S. Liu, T.C. Cheng, W.C. Chang, and S.K. Lo, *Energy Conversion and Management*, 62 (2012) 14.
10. S. Toghyani, E. Afshari, and E. Baniasadi, *Electrochimica Acta*, 290 (2018) 506.
11. Y. Vazifeshenas, K. Sedighi, and M. Shakeri, *Applied Thermal Engineering,* 147 (2019) 81.
12. K. Roßberg, and V. Trapp, *Handbook of Fuel Cells*, (2010).
13. C.E. Lu, N.W. Pu, K.H. Hou, C.C. Tseng, and M.D. Ger, *Applied surface science*, 282 (2013) 544.
14. Z. Chen, G. Zhang, W. Yang, B. Xu, Y. Chen, X. Yin, and Y. Liu, *Chemical Engineering Journal*, (2020) 124675.
15. JJ. Hwang, MM. Dlamini, FB. Weng, T. Chang, CH. Lin, SC. Weng, *Energy*, 244 Part A (2021) 122714.
16. L.X. Yang, R.J. Liu, Y. Wang, H.J. Liu, C.L. Zeng, and C. Fu, *Corrosion Science*, 174 (2020) 108862.
17. S.B. Lee, K.H. Cho, W.G. Lee, and H. Jang, *J. Power Sources*, 187(2009) 318.
18. K. Lin, X. Li, L. Tian, and H. Dong, *international journal of hydrogen energy*, 40 (2015) 10281.
19. A. Miyazawa, E. Tada, and A. Nishikata, *J. power sources*, 231 (2013) 226.
20.   Z. Niu, L. Fan, Z. Bao, and K. Jiao, *International Journal of Energy Research*, 42(2018) 3328.
21. Z. Bao, Z. Niu, and K. Jiao, *J. Power Sources,* 438 (2019) 226995.
22. J. Kim, G. Luo, and C.Y. Wang, *J. Power Sources*, 365 (2017) 419.
23. H.J. Bong, J. Lee, J.H. Kim, F. Barlat, and M.G. Lee, *International Journal of Hydrogen Energy*, 42 (2017) 6965.
24. M.M. Barzegari, and F.A. Khatir, *International Journal of Hydrogen Energy*, 44 (2019) 31360.
25. L. Peng, X. Lai, P. Yi, J. Mai, and J. Ni, *Journal of Fuel Cell Science and Technology*, 8 (2011).
26. L. Belhassen, S. Koubaa, M. Wali, and F. Dammak, *International Journal of Mechanical Sciences*, 117 (2016) 218.
27. W. Hongyu, T. Fei, W. Zhen, Z. Pengchao, S. Juncai, and J. Shijun, *Journal of Manufacturing Processes*, 40 (2019) 94.
28. H. Kargar-Pishbijari, S.J. Hosseinipour, and H.J. Aval, *Journal of Manufacturing Processes*, 55 (2020) 268.
29. A. Malekian, S. Salari, J. Stumper, N. Djilali, and M. Bahrami, *International Journal of Hydrogen Energy*, 44 (2019) 23396.
30. T. Zhang, D. Shen, S. Zheng, Z. Liu, X. Qu, and D. Tao, *International Journal of Industrial Ergonomics*, 80 (2020) 103047.
31. K. Karacan, S. Celik, S. Toros, M. Alkan, and U. Aydin, *International Journal of Hydrogen Energy*, 45 (60) (2020) 35149-35161
32. T. Wilberforce, Z. El-Hassan, F.N. Khatib, A. Al Makky, J. Mooney, A. Barouaji, J.G. Carton, and A.G. Olabi, *International journal of hydrogen energy*, 42 (2017) 25663.
33. R. Boddu, U.K. Marupakula, B. Summers, and P. Majumdar, *J. Power Sources*, 189 (2009) 1083.
34. T. Chen, S. Liu, S. Gong, and C. Wu, *International journal of energy research*, 37 (2013) 1680.
35. T. Yoshida, and K. Kojima, *The Electrochemical Society Interface*, 24 (2015) 45.
36. H. Heidary, M.J. Kermani, and B. Dabir, *Energy Conversion and Management*, 124 (2016) 51.
37. C.S. Kim, J. Jung, J.H. Jang, H.J. Kim, H.S. Park, J.W. Kang, Y. Na, and H.Y. Park, *International Journal of Hydrogen Energy*, 45 (2020) 32808.
38. S. Ouyang, C. Li, L. Du, X. Li, Z. Lai, T. Peng, X. Han, Q. Cao, and L. Li, *Journal of Materials Processing Technology*, 291 (2020) 117001.
39. M. Chen, Z. Lai, Q. Cao, X. Han, C. Wang, N. Liu, and L. Li, *Journal of Manufacturing Processes*, 57 (2020) 209.

40. Q.J. ZHAO, C.J. WANG, H.P. YU, G.U.O. Bin, D.B. SHAN and C.F. LI, *Transactions of Nonferrous Metals Society of China*, 21 (2011) s461.
41. S. Xu, K. Li, Y. Wei, and W. Jiang, *International Journal of Hydrogen Energy*, 41 (2016) 6855.
42. A. Alaswad, A.G. Olabi, and K.Y. Benyounis, *Materials & Design,* 32(2011) 838.
43. C. Zhang, J. Ma, X. Liang, F. Luo, R. Cheng, and F. Gong, *Journal of Materials Processing Technology*, 262 (2018) 32.
44. B. Abeyrathna, P. Zhang, M.P. Pereira, D. Wilkosz, and M. Weiss, *International Journal of Hydrogen Energy*, 44 (2019.) 3861.
45. M. Elyasi, H.T. Ghadikolaee, and M. Hosseinzadeh, *The International Journal of Advanced Manufacturing Technology*, 92 (2017) 765.
46. H.T. Ghadikolaee, M. Elyasi, F.A. Khatir, and M. Hosseinzadeh, *Procedia engineering*, 207 (2017) 1647.
47. R. Kolahdooz, S. Asghari, S. Rashid-Nadimi, and A. Amirfazli, *International Journal of Hydrogen Energy*, 42 (2017) 575.
48. C. Zhang, J. Ma, X. Liang, F. Luo, R. Cheng, and F. Gong, *Journal of Materials Processing Technology*, 262 (2018) 32.
49. R. Zhang, S. Lan, Z. Xu, D. Qiu, and L. Peng, *J. Power Sources*, 484 (2021) 229298.
50. H. Talebi-Ghadikolaee, M. Elyasi, and M.J. Mirnia, *Thin-Walled Structures*, 150 (2020) 106671.
51. F.A. Khatir, M. Elyasi, H.T. Ghadikolaee, and M. Hosseinzadeh, *Procedia Engineering*, 183, (2017) 322.
52. C.K. Jin, M.G. Jeong, and C.G. Kang, *International Journal of Hydrogen Energy*, 39(2014) 21480.
53. K.H. Lee, C.K. Jin, C.G. Kang, H.Y. Seo, and J.D. Kim, *Fuel Cells*, 15 (2015) 170.
54. S. Esmaeili, and S.J. Hosseinipour, *SN Applied Sciences*, 1 (2019) 187.
55. G. Giuliano, and W. Polini, *Manufacturing Letters*, 24 (2020) 72.
56. M.K. Choi, H. Huh, and N. Park, *Journal of Materials Processing Technology*, 244 (2017) 331.
57. J.C. Hung, and C.C. Lin, *J. Power Sources*, 206 (2012) 179.
58. Z. Xu, L. Peng, P Yi, and X. Lai, International Journal of Mechanical Sciences, 150 (2019) 265.
59. L. Jiang, J.A. Syed, G. Zhang, Y. Ma, J. Ma, H. Lu, and X. Meng, *Journal of Industrial and Engineering Chemistry*, 80 (2019) 497.
60. N.F. Asri, T. Husaini, A.B. Sulong, E.H. Majlan, and W.R.W. Daud, *International Journal of Hydrogen Energy*, 42 (2017) 9135.
61. R.Y. He, J. Jiang, R.F. Wang, Y. Yue, Y. Chen, and T.J. Pan, *Corrosion Science*, (2020) 108646.
62. S. Liu, T.J. Pan, R.F. Wang, Y. Yue, and J. Shen, *Progress in Organic Coatings*, 136 (2019) 105237.
63. J.L. Lu, N. Abbas, J. Tang, R. Hu, and G.M. Zhu, *Electrochemistry Communications*, 105 (2019) 106490.
64. A.P. Manso, F.F. Marzo, X. Garicano, C. Alegre, A. Lozano, and F. Barreras, *International Journal of Hydrogen Energy*, 45 (2020) 20679.
65. A.V. Ingle, V.S. Raja, J. Rangarajan, and P. Mishra, *International Journal of Hydrogen Energy*, 45 (2020) 3094.
66. P. Gao, Z. Xie, X. Wu, C. Ouyang, T. Lei, P. Yang, C. Liu, J. Wang, T. Ouyang, and Q. Huang, *International Journal of Hydrogen Energy*, 43 (2018) 20947.
67. U.K. Chanda, A. Behera, S. Roy, and S. Pati, *International Journal of Hydrogen Energy*, 43 (2018) 23430.
68. E. Haye, F. Deschamps, G. Caldarella, M.L. Piedboeuf, A. Lafort, H. Cornil, J.F. Colomer, J.J. Pireaux, and N. Job, *International Journal of Hydrogen Energy*, 45 (2020) 15358.
69. L.X. Yang, R.J. Liu, Y. Wang, H.J. Liu, C.L. Zeng, and C. Fu, *Corrosion Science*, 174 (2020) 108862.

70. Z. Sadeghian, M.R. Hadidi, D. Salehzadeh, and A. Nemati, *International Journal of Hydrogen Energy*, 45 (2020) 15380.
71. F. Madadi, A. Rezaeian, H. Edris, and M. Zhiani, *Materials Chemistry and Physics*, 238 (2019) 121911.
72. J.A. Syed, S. Tang, and X. Meng, *Scientific reports*, 7 (2017) 1.
73. Y. Wang, S. Zhang, P. Wang, Z. Lu, S. Chen, and L. Wang, *Progress in Organic Coatings*, 137 (2019) 105327.
74. I. Alaefour, S. Shahgaldi, J. Zhao, and X. Li, *International Journal of Hydrogen Energy*, 46 (2021) 11059.
75. P. Yan, T. Ying, Y. Li, D. Li, F. Cao, X. Zeng, and W. Ding, *J. Power Sources*, 484 (2021) 229231.
76. Z. Wang, K. Feng, Z. Li, F. Lu, J. Huang, Y. Wu, and P.K. Chu, *international journal of hydrogen energy*, 41 (2016.) 5783.
77. S.H. Lee, N. Kakati, J. Maiti, S.H. Jee, D.J. Kalita, and Y.S. Yoon, *Thin Solid Films*, 529 (2013) 374.
78. D. Özkan, *Wear*, 454 (2020) 203344.
79. A. Kumar, H. Batham, and A.K. Das, *Materials Today: Proceedings*, 39 (2021) 1291.
80. E.E. Kahveci, and I. Taymaz, *Fuel*, 253 (2019) 1274.
81. J. Shi, P. Zhang, Y. Han, H. Wang, X. Wang, Y. Yu, and J. Sun, *International Journal of Hydrogen Energy,* 45 (2020) 10050.
82. L. Wang, Y. Tao, Z. Zhang, Y. Wang, Q. Feng, H. Wang, and H. Li, *International Journal of Hydrogen Energy*, 44(2019) 4940.
83. T.S.K. Raunija, *Ceramics International*, 41 (2015) 6340.
84. https://www.electrical4u.com/electrical-resistance-and-laws-of-resistance/(last visited 17/01/2021)
85. V. Ammosov, V. Korablev, and V. Zaets, *Nuclear Instruments and Methods in Physics Research Section A: Accelerators, Spectrometers, Detectors and Associated Equipment*, 401 (1997) 217.
86. C. Adelmann, *Solid-State Electronics*, 152 (2019) 72.
87. T. Wilberforce, O. Ijaodola, E. Ogungbemi, F.N. Khatib, T. Leslie, Z. El-Hassan, J. Thompson, and A.G. Olabi, *Renewable and Sustainable Energy Reviews*, 113 (2019) 109286.
88. M.M. Sisan, M.A. Sereshki, H. Khorsand, and M.H. Siadati, *Journal of alloys and compounds*, 613 (2014) 288.
89. M.A. Deyab, *J. Power Sources*, 268 (2014) 50.
90. H. Wang, M.A. Sweikart, and J.A. Turner, *J. Power Sources*, 115 (2003) 243.
91. K. Lin, X. Li, Y. Sun, X. Luo, and H. Dong, *International journal of hydrogen energy*, 39 (2014) 21470.
92. H. Husby, O.E. Kongstein, A. Oedegaard, and F. Seland, *International journal of hydrogen energy*, 39 (2014) 951.
93. D.P. Davies, P.L. Adcock, M. Turpin, and S.J. Rowen, *Journal of Applied Electrochemistry*, 30 (2000) 101.
94. https://kta.com/kta-university/adhesion-astm-d3359/(last visited 18/02/2021)
95. https://www.energy.gov/sites/prod/files/2017/11/f46/fcto_biploar_plates_wkshp_report.pdf (last visited 06/01/2021)
96. Y. Song, C. Zhang, C.Y. Ling, M. Han, R.Y. Yong, D. Sun, and J. Chen, *International Journal of Hydrogen Energy*, 45 (2020) 29832.
97. P. Zhang, M. Pereira, B. Rolfe, W. Daniel and M. Weiss, Deformation in micro roll forming of bipolar plate, *J. Phys.: Conf. Ser.* 896 (2017) 012115
98. A. Bauer, S. Härtel, and B. Awiszus, *Journal of Manufacturing and Materials Processing*, 3 (2019) 48.

99.   N. Keller, A. Bauer, T. von Unwerth, and B. Awiszus, *Journal of Manufacturing and Materials Processing*, 4 (2020) 1.
100. J. Huang, Y. Deng, P. Yi, and L. Peng, *The International Journal of Advanced Manufacturing Technology*, 100 (2019) 117.
101. R. Zhang, S. Lan, Z. Xu, D. Qiu, and L. Peng, *J. Power Sources*, 484 (2021) 229298.
102. L. Qin, W.L. Yue, and C.J. Luo, In *Applied Mechanics and Materials*, 442 (2014) 269.